iScience

CellPress
OPEN ACCESS

Article

Attaching organic fibers to mineral: The case of the avian eggshell

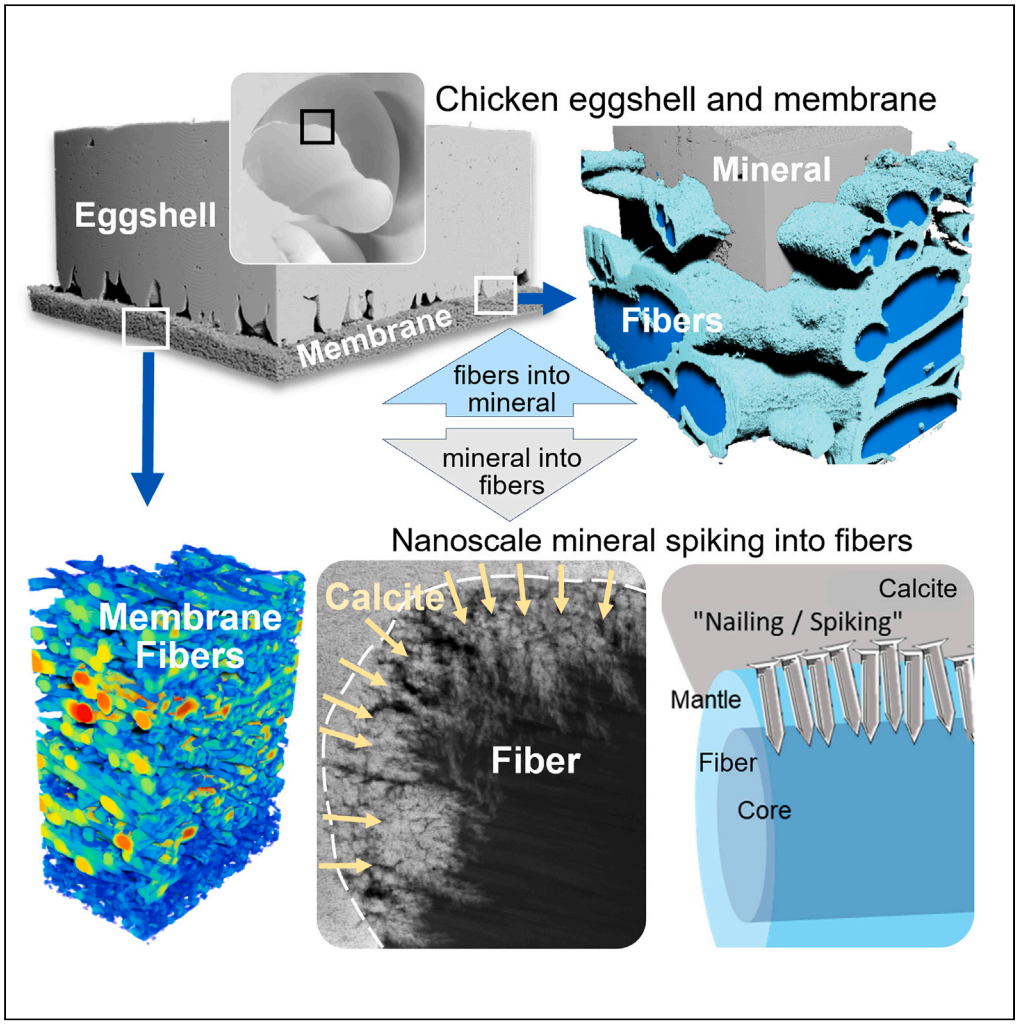

Daniel J. Buss, Natalie Reznikov, Marc D. McKee

marc.mckee@mcgill.ca

Highlights

Avian eggshell mineral and their underlying membrane fibers reciprocally integrate

A two-way multiscale anchorage system interfaces organic fibers with calcitic mineral

Fibers embed into mineral at the microscale, and mineral into fibers at the nanoscale

Shell mineral spiking into fibers increases surface area for robust membrane attachment

Buss et al., iScience *26*, 108425
December 15, 2023
https://doi.org/10.1016/j.isci.2023.108425

iScience

CellPress
OPEN ACCESS

Article

Attaching organic fibers to mineral: The case of the avian eggshell

Daniel J. Buss,[1] Natalie Reznikov,[1,2,3] and Marc D. McKee[1,3,4,*]

SUMMARY

Bird eggs possess a mineralized eggshell with a soft underlying fibrous membrane. These dissimilar material layers successfully evolved a structural attachment to each other as a conserved avian reproduction strategy essential to avian embryonic development, growth, and hatching of the chick. To understand how organic membrane fibers attach to shell mineral (calcite), 3D multiscale imaging including X-ray and electron tomography coupled with deep learning-based feature segmentation was used to show how membrane fibers are organized and anchored into shell mineral. Whole fibers embed into mineral across the microscale, while fine mineral projections (granules/spikes) insert into fiber surfaces at the nanoscale, all of which provides considerable surface area and multiscale anchorage at the organic-inorganic interface between the fibrous membrane and the shell. Such a reciprocal anchorage system occurring at two different length scales between organic fibers and inorganic mineral provides a secure attachment mechanism for avian eggshell integrity across two dissimilar materials.

INTRODUCTION

Avian eggshell formation is one of the fastest biomineralization processes known, where a fully formed highly organized calcified structure (with traversing pores for gas and water vapor exchange[1–3]) arises within 20 h from a template of organic fibers.[4] Mineralized eggshell formation occurs in the shell gland segment (uterus) of the hen's oviduct but is preceded by the assembly of an organic eggshell membrane at the surface of the egg "white" as the egg transits through the oviduct.[4,5] The membrane – which eventually becomes attached to the innermost portion of the shell – is formed predominantly of an interconnected and branching meshwork of fibers.[6–9] Compositionally, the membrane consists of approximately 250 proteins, namely, various collagens,[10–14] cystine-rich eggshell membrane proteins (CREMPs), and other proteins and biomolecules including those with known antimicrobial function, such as lysozyme.[15–19] The presence of distinct organic sulfate species has also been demonstrated in the membrane.[20] Nucleation of the shell's calcium carbonate mineral originates on and between the outermost membrane fibers, beginning as an amorphous phase, and then growing and maturing toward calcite.[17,21,22] This mineralization trajectory starts with the formation of quasiperiodic mineral aggregates on the outer membrane. Growing outwards from the incipient aggregates, so-called mammillae are formed, altogether constituting the innermost mammillary layer of the shell.[4,8,9,21,23,24] Rapid, confluent columnar calcite growth then proceeds further outwards from each mammilla as densely packed calcite columns, resulting in a contiguous array that also contains radially arranged pores.[1,2,4,19] This process occurring in the shell gland of the oviduct produces close to 5 g of calcite[22] to reach a final shell thickness of approximately 300–350 μm in chicken eggs.

After a fertilized egg is laid, secure attachment of the outer membrane fibers to the mammillae is essential for successful development of the chick. With egg incubation, by embryonic day 15, a fully developed, cellular and vascularized chorioallantoic membrane (CAM) lying immediately beneath the membrane[7,25] mediates significant dissolution of the shell to mobilize calcium from mammillary calcite for the growing chick skeleton through acidification mechanisms acting across the membrane.[26,27] Secure attachment of the membrane to the shell is therefore required to approximate the underlying CAM close to the shell to facilitate shell dissolution and calcium release.[25–27] Toward the end of CAM-mediated shell dissolution, the outer eggshell membrane partially detaches from the shell,[25,26,28] potentially contributing to shell weakening for the emergence of the chick (pipping). Related to this, an intact eggshell membrane attachment has been implicated as a contributor to shell mechanical strength.[29,30]

While the congruent, the trilaminar structure of the CAM, the membrane, and the shell constitutes the typical egg "wall," at the blunt end of the egg, something substantially different occurs.[4] In the blunt region, the membrane splits to form the air sac – this occurring after the egg is laid and begins to cool, drawing in air through the pores of that region.[1–3] Once formed, the air sac provides a reservoir to meet the developing chick's growing oxygen demand before and at the time of hatching.[2,3]

[1]Department of Anatomy and Cell Biology, School of Biomedical Sciences, Faculty of Medicine and Health Sciences, McGill University, Montreal, QC H3A 0C7, Canada
[2]Department of Bioengineering, Faculty of Engineering, McGill University, Montreal, QC H3A 0E9, Canada
[3]Faculty of Dental Medicine and Oral Health Sciences, McGill University, Montreal, QC H3A 0C7, Canada
[4]Lead contact
*Correspondence: marc.mckee@mcgill.ca
https://doi.org/10.1016/j.isci.2023.108425

For unfertilized and unincubated "table eggs" stored in a variety of conditions and used as a major food source across most populations, food safety is of concern.[31] The intact membrane is a major physical and antimicrobial defense barrier for the egg contents,[15] and detachment of the membrane from the shell in eggs may render them more susceptible to contamination from opportunistic microorganisms.[31,32] The present study was undertaken to provide a better fundamental understanding of how such an important and robust attachment is achieved at this interface between overall strikingly dissimilar materials – organic fibers and biomineral.

RESULTS

3D multiscale imaging of chicken eggshell membrane structure

To date, avian eggshell membrane structure has primarily been studied using light microscopy, scanning electron microscopy (SEM), and transmission electron microscopy (TEM) of conventionally prepared specimens (critical-point dried, aldehyde-fixed).[6,7,9] Here, we expand upon this largely 2D information to a 3D multiscale assessment of the chicken (*Gallus gallus domesticus*) eggshell membrane and its interface with the shell (Figures 1 and 2, Videos S1 and S2).

The organic fibrous membrane attaches to mammillae of the calcitic shell (Figures 1A and 1C, Videos S1 and S2). Using deep learning-based segmentation and thickness mapping of membrane fibers from submicrometer microcomputed tomography (μCT) volumes, small-diameter inner membrane fibers, and large-diameter outer membrane fibers, were differentiated (Figure 1B, n=5, representative areas shown). For higher-resolution examination of the membrane fibers, precise focused-ion beam (FIB) milling in conjunction with SEM imaging (particularly using backscattered electron imaging in the serial-surface-view [SSV] mode) has recently provided enhanced understanding of 3D nano-to microscale relationships in a variety of mineralized fibrous biocomposites.[33–35] Using serial gallium-FIB milling tangential to the membrane, and imaging using backscattered electron detection, we assessed the 3D structure of a complete thickness of the membrane. Using fiber thickness mapping at this scale (Figures 1D and Videos S3 and S4), the outer and inner membrane layers were visualized in detail with an abrupt shift to thin fibers within the approximate inner 15 μm of the membrane (toward the egg albumen). Directionality mapping of fibers through the membrane (Figure 1E) revealed orthotropic, mat-like fiber orientation.

An important morphological feature of eggshell membrane fibers when imaged using an electron microscope (and typically stained) are inner core and outer mantle regions of each fiber[6] (Figures 2A and Video S5). This mantle region of eggshell membrane fibers is distinct from, and should not be confused with, the mantle cellular tissue in invertebrate organisms such as mollusks and brachiopods. From several 3D volumes of the eggshell membrane fibers, we were able to reveal oblique projections at both the micro- (Figure 2C) and nanoscales (Figure 2D) that document a previously uncommunicated propensity of chicken eggshell membrane fibers to form bundles (some up to 50 μm in width and several up to 100 μm in length), with a shared mantle region and discrete core regions (Figures 2C and 2D). Segmentation of core and mantle fiber regions through the membrane thickness suggests that the inner membrane, with smaller overall fiber diameters, indeed has a reduced proportion of core organic constituents compared to that of larger outer membrane fibers, whereas the mantle proportion is rather similar in both thin and thick fibers (Figures 2B and Video S5).

Attaching organic fibers to biomineral at the eggshell-membrane interface

Having obtained a broader understanding of overall membrane fiber morphologies (including mantle and core regions) and orientation, we addressed unresolved questions regarding the morphology of fiber incorporation (of both embedded fibers and interdigitated fibers) in the mammillary calcite.[9,23,24] Collectively, compelling evidence is provided for a self-affine, reciprocal anchorage of organic fibers at both the micro- and nanoscale. First, at the microscale, about 10 fibers are anchored into each mammilla (Figures 3A and 3B, Video S6). Deep learning-assisted segmentation of these fibers within mammillae calcite (Figures 3B and 3C) revealed that all mammillae in the field of view (between 200 and 300 mammillae per 1 mm^2 area of shell[36]) contained anchored fibers (Figure 3C).

At higher resolution (FIB-SEM reconstructions), using 3D segmentation of a portion of a mammilla (from the same volume as Figure 1), multiple fiber tracks (about ten per mammilla) can be revealed by digitally removing the fibers (Figure 3D and Video S7). Two additional volumes at even higher resolutions (Figures 3E and 3F, Video S8) show the difference of the mantle texture around embedded and interdigitated fibers – namely uniformly thin mantles having a rough irregular texture when embedded, compared to the thicker mantles of the interdigitated fibers. In addition, a different 3D structure of the fiber mantle regions was observed (Figure 3E rightmost image; Figure 4D, Video S8). Segmentation and thickness mapping of embedded and interdigitated mantle regions reveals that the mantle area is occluded with mineral extensions into the fiber, supported by backscattered electron signal intensity which is instead consistent with the shell mammillary calcite (Figures 3F and 4A). Indeed, these embedded fibers, including where they stretch between adjacent mammillae, remain attached after manually peeling off the membrane (Figure S3).

Sections of interdigitated fibers cut using a microtome and imaged under TEM brightfield conditions previously indicated (based on electron density and shape) that a mineral phase within fiber mantles is likely responsible for these radial inhomogeneities in the mantle.[9] Still, the suggested mineral polymorph and 3D morphology of anchored fiber mantles has not been assessed in the context of membrane-shell attachment – this likely being attributable to the extreme difficulty and lack of precision in cutting hard and brittle shells with a microtome. To address this, FIB milling of a conventionally fixed and osmium stained electron-transparent section (lamella) of a mammilla with its embedded fibers was conducted for further observations by STEM (scanning transmission electron microscopy). Using selected-area diffraction (SAED) (Figure 4F), we observed only diffuse reflections of the mineral penetrating into the fiber mantle, this in contrast to mammillary mineral showing regular bright spot reflections indicative of single-crystal calcite. This observation of poorly crystalline mineral penetrating into

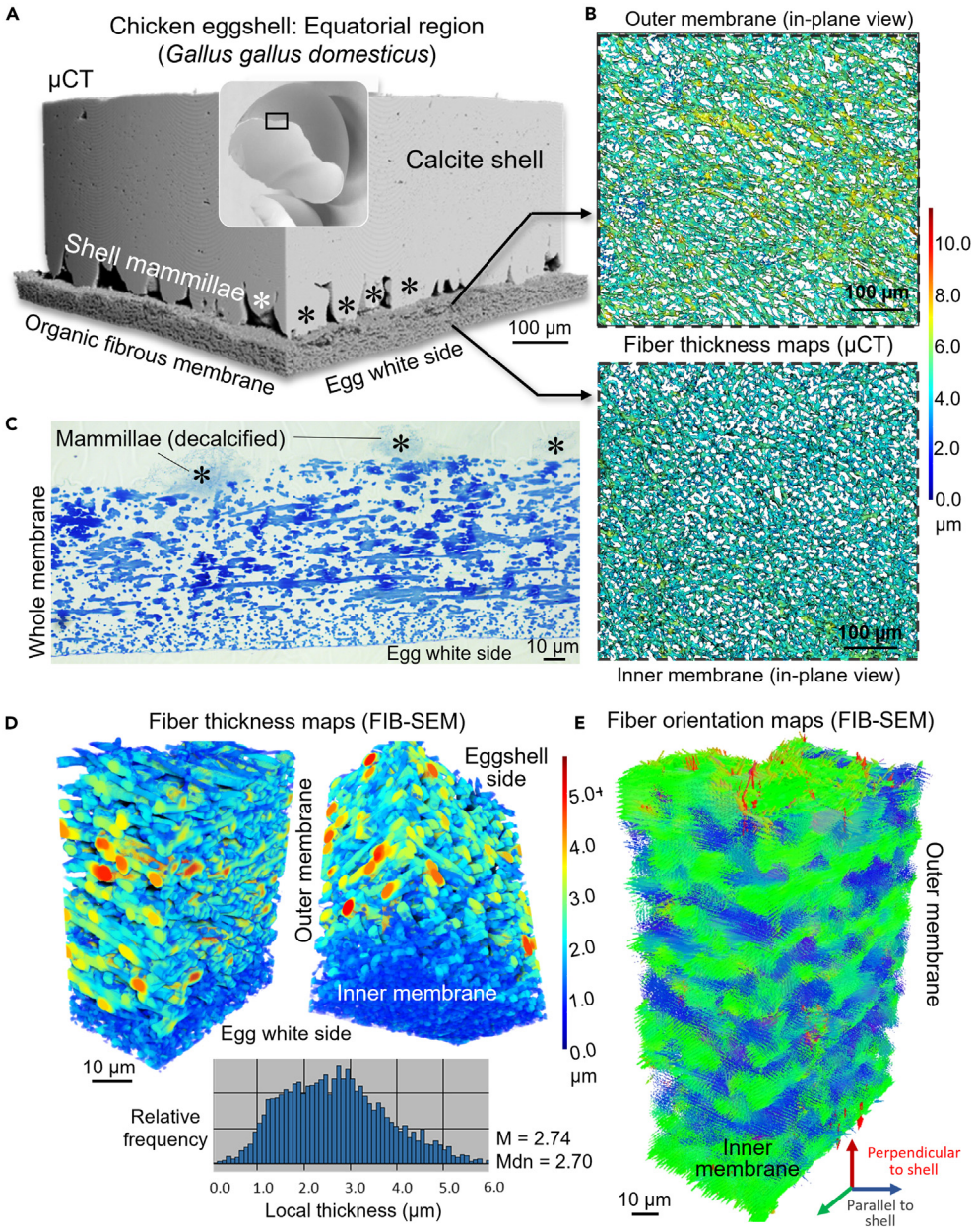

Figure 1. Chicken eggshell membrane fibers by submicrometer μCT and FIB-SEM microscopy

(A) μCT and segmentation of a complete shell and eggshell membrane cross-section from the equatorial region of an egg. Shell mammillae (*) form from initial mineral nucleation and growth at the outer membrane surface (see Videos S1 and S2).

(B) Thickness mapping of digitally prepared sections of outer and inner membrane fibers showing fiber size differences over large fields of view.

(C) Light micrograph of a toluidine blue-stained section of full-thickness eggshell membrane. Mammilla (here decalcified, no mineral) are denoted by asterisks.

(D) Thickness mapping of a gallium FIB-SEM serial-surface-view reconstruction of a full-thickness eggshell membrane, with the corresponding distribution of fiber thicknesses. A portion of an adjacent calcitic mammilla was segmented and digitally removed, but can be seen in Video S3 (registered slices), Video S4 (thickness map), and Video S7 (mammilla detailed).

(E) Mapping of local fiber directionality showing orthotropic assembly through the same full eggshell membrane 3D cross-section.

the mantle was supported by similarly prepared specimens imaged using angle-selective (BSE-L) and energy-selective (BSE-U) detectors from our high-resolution FIB-SEM volumes in which isolated bright electron-dense spots were observed within the mantle voids (Figure 4D).

Given the high surface-to-volume ratio of the fine mineral extensions, and the known solubility of certain precursor phases of calcium carbonate in water, we next FIB-milled an electron-transparent section (lamella) through a mammilla region with embedded fibers from a

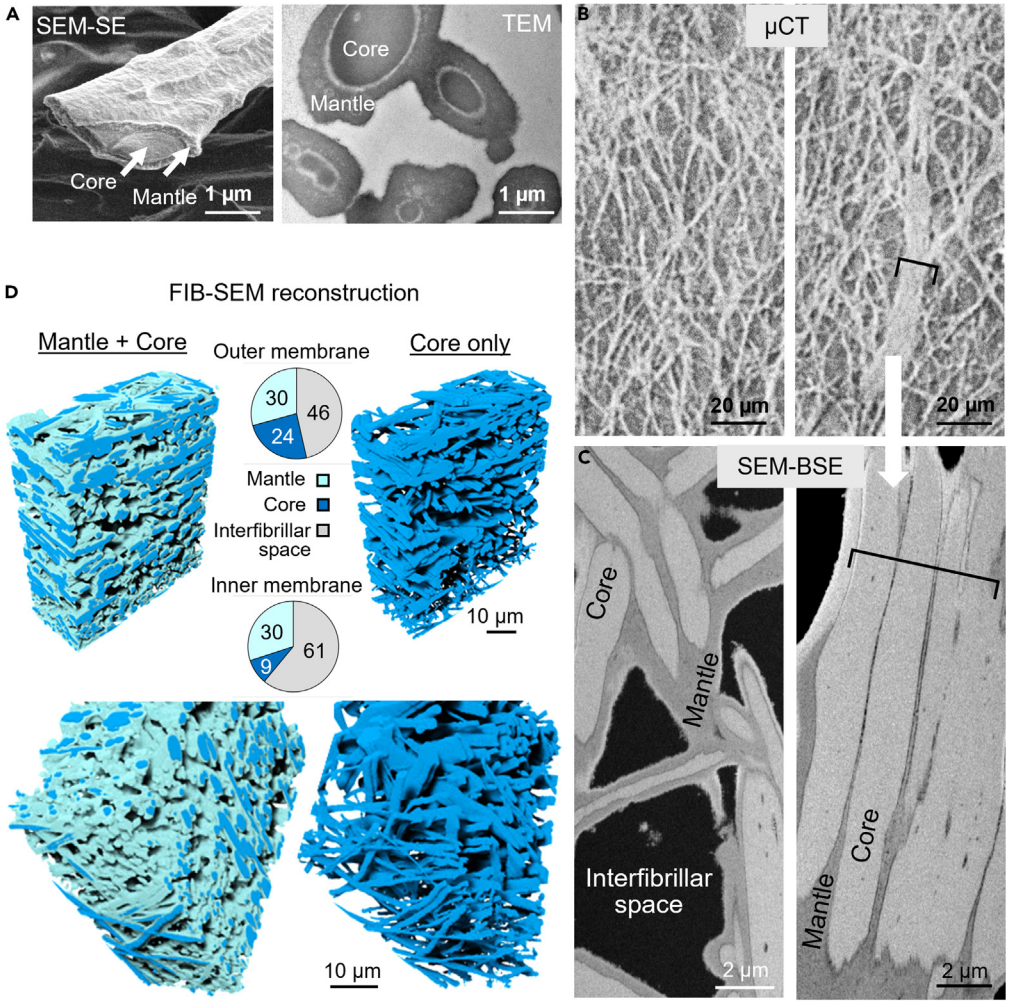

Figure 2. Fiber mantle and core morphologies assessed correlatively and in 3D

(A) SEM and TEM electron microscopy images showing distinctions typical of mantle and core eggshell membrane fiber regions in topographical and stained section micrographs.

(B and C) Correlation of oblique projections of outer membrane fibers from µCT (B) and SEM-BSE (C) showing regions of both isotropic fibers and also large fiber bundles (brackets) with significant similar directionality and size within the outer membrane. Fiber bundles exist as arrays of sandwiched mantle and core constituents.

(D) FIB-SEM serial-surface-view deep learning-based segmentation of fiber mantle (turquoise) and core (blue) through a near-full-thickness membrane (Video S5). While mantle volume fractions are the same in the outer and inner membranes, the core volume fraction within the inner membrane is reduced.

cryo-fixed specimen. Cryo-preparation of samples (high-pressure freezing followed by freeze-substitution) results in better preservation of hydrated mineral phases, including unstable amorphous mineral precursor phases.[37] SAED patterns collected from the now cryo-prepared fiber mantle (Figure 4G) instead revealed an arching diffraction pattern indicative of polycrystalline calcite texture. This finding was corroborated by STEM high-angle annular dark field imaging (Figures 4B,4C, and 4E). With the preservation enabled by cryo-processing and ultrafine ion-beam milling, two unique mantle mineral morphologies were captured – polycrystalline "granules" in the embedded fiber mantles (Figure 4C) and "spikes" in the interdigitated fiber mantles (Figure 4E). Energy-disperse spectroscopy (EDS) spectra confirmed the presence of calcium (Figure 4H) and oxygen (Figure 4I) within these mammilla-anchored fiber mantles (compared to fiber core regions where there was little calcium or oxygen signal), and where there was a similar intensity as mammilla calcite itself (Figures 4H and 4I, at the top of each map). These analytical data show that mantle "voids" in conventionally prepared specimens (Figure 4D and Video S8) are indeed decalcified proxy spaces occupied in their entirety in native eggshell by polycrystalline mineral spikes or granules (Figure 4E). In addition, by taking together results from the FIB-SEM high-resolution 3D segmentation, the osmium-stained conventionally prepared lamella, and the cryo-prepared lamella, we now have shown how mineral "spikes" (of up to 100 nm in thickness and 500 nm in length) indeed penetrate into the mantle radially and extend partially into even the inner core of membrane fibers (Figures 4J and 5, Video S9).

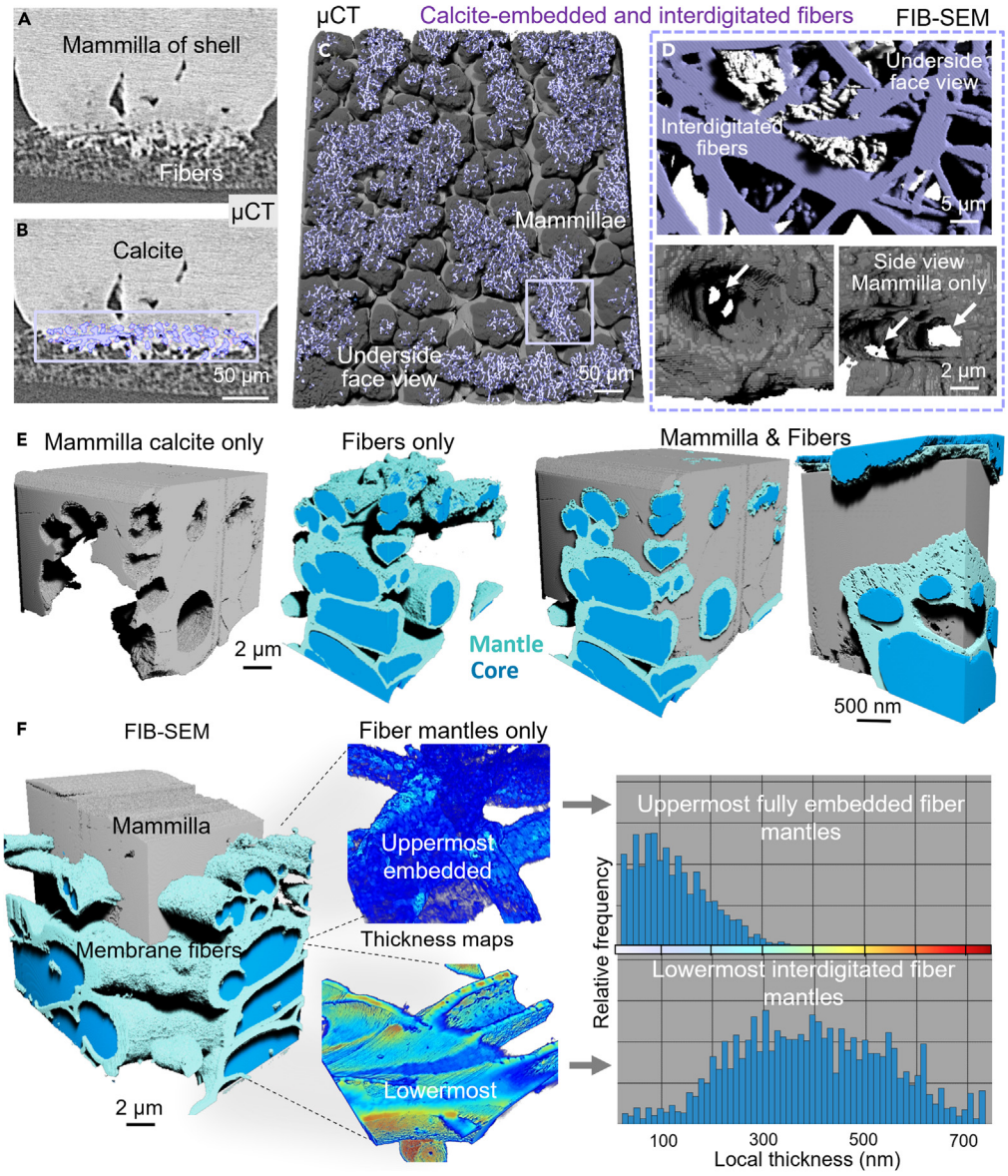

Figure 3. Attachment of interdigitated eggshell membrane fibers to the shell across the microscale: Ubiquitous and progressive embedding of fibers within calcitic shell mammillae

(A) During initial mineralization to form the eggshell, outermost membrane fibers become embedded within calcitic mammillae. μCT analysis.

(B) Deep learning was used to segment only mammilla-anchored fibers (purple) that are either completely embedded or interdigitated with mammilla calcite. μCT analysis.

(C) Multiple fibers are anchored to all mammillae, thus attaching the membrane to the shell. μCT and FIB-SEM analysis.

(D) FIB-SEM serial-surface-view and segmentation of calcite mineral (gray) and fibers (purple) reveals tracts where fibers are anchored to the mammilla (Video S7).

(E) At higher resolution in different reconstructed FIB-SEM volumes, both embedded and interdigitated fibers are observed, showing distinct morphologic features.

(F) The mantles of the completely embedded uppermost fibers are thin and uniform, whereas the mantles of the interdigitated fibers are nonuniform and have higher thicknesses.

To estimate the extent of the anchorage of the membrane fibers to the shell mammillae, a coarse-grained calculation can be applied as follows. The surface area of an average-sized chicken egg is approximately 7,000 mm^2 (70 cm^2) consistent with the reported surface area from Narushin and Paganelli.[38,39] Next, the number of mammillae per square millimeter varies between 180 and 300 (being more numerous in younger hens[36]), which gives a conservative estimate of about 1.3 million mammillae per egg. The diameter of a typical mammilla at the level of the membrane anchorage is usually slightly exceeding 100 μm^2. With an average of approximately 10 fibers being anchored to each

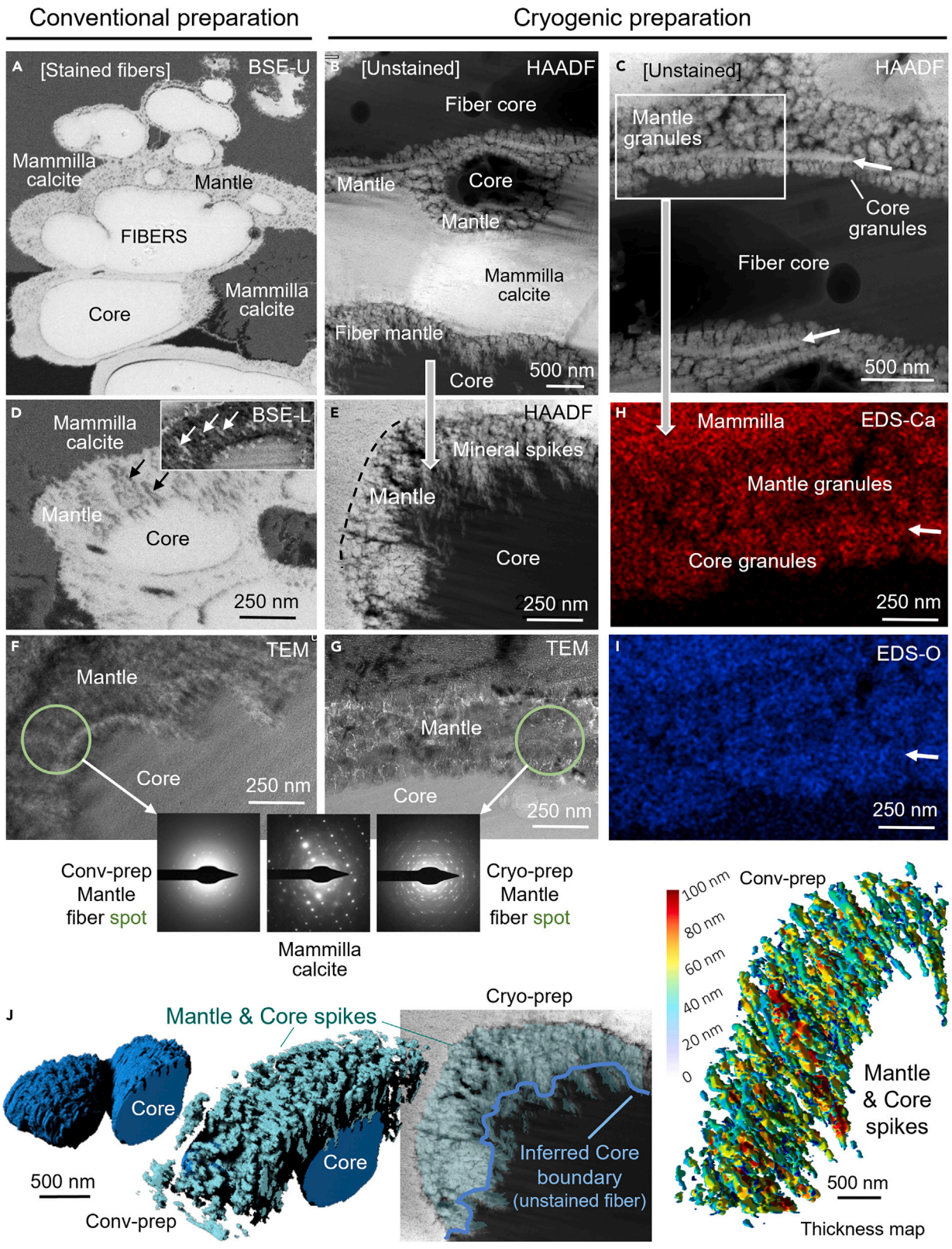
Conventional preparation
Cryogenic preparation
A
[Stained fibers]
BSE-U
Mammilla calcite
Mantle
FIBERS
Core
Mammilla calcite
B
[Unstained]
HAADF
Fiber core
Mantle
Core
Mantle
Mammilla calcite
Fiber mantle
Core
500 nm
C
[Unstained]
HAADF
Mantle granules
Core granules
Fiber core
500 nm
D
Mammilla calcite
BSE-L
Mantle
Core
250 nm
E
HAADF
Mineral spikes
Mantle
Core
250 nm
H
Mammilla
EDS-Ca
Mantle granules
Core granules
250 nm
F
TEM
Mantle
Core
250 nm
G
TEM
Mantle
Core
250 nm
I
EDS-O
250 nm
Conv-prep Mantle fiber spot
Mammilla calcite
Cryo-prep Mantle fiber spot
J
Mantle & Core spikes
Core
Core
500 nm
Conv-prep
Cryo-prep
Inferred Core boundary (unstained fiber)
100 nm
80 nm
60 nm
40 nm
20 nm
0
Conv-prep
Mantle & Core spikes
500 nm
Thickness map

Figure 4. Attachment of eggshell membrane fibers to the shell at the nanoscale: Multiscale assessment of fiber mineral granules and spikes

Transient amorphous mineral phases at fine dimensions are sensitive to aqueous-based conventional sample-preparation techniques.[37] After acquiring several FIB-SEM volumes that were conventionally processed and stained (A, D, F, and J) – versus cryo-prepared (B, C, E, and G–J) – BSE differences in contrast suggested that within fiber mantles that adopt the more porous "void-like" morphology (D, black arrows, also see Video S8), there was in fact propagation of small mineral spots/streaks (D, white arrows in inset). Diffuse electron diffraction reflections after SAED of fiber mantle from a FIB-prepared lamella of the same sample corroborated that these were mostly voids with small amounts of mineral (F). For better characterization of the mammilla-embedded and interdigitated fiber mantle "voids" that shows some evidence of mineral, an additional lamella (B, C, E, and G–I) was prepared using cryo-conditions to preserve mineral, namely high-pressure freezing and freeze substitution. STEM/HAADF imaging of this lamella revealed two previously unrecognized mineral morphologies (B) – mineral "granules" present in embedded fiber mantles (C), and mineral "spikes" of interdigitated fiber mantles (E), with the spikes often being hundreds of nanometers in length. Electron diffraction of fiber mantle mineral from this cryo-prepared specimen was indicative of polycrystalline calcite (G), with much stronger reflections than that after conventional aqueous preparation, but distinct from single-crystal calcite of the mammillae. These data were further corroborated by EDS showing abundant Ca and O within the mantle (H, I). A thin mineralized layer was also observed at the interface between the fiber core and mantle (white arrows in panels C, H, and I) in the cryo-prepared samples, which appeared as a narrow void/gap in the conventionally prepared samples (A, D). Stained, conventionally prepared samples consistently show fiber voids extending into the core region of the fibers (D, F, Video S8), and a gap between mantle and core regions (D, F), where mineral was found in cryo-prepared samples (C, H, I). Taking both preparations together, these results indicate that fiber voids (D, J) from conventionally prepared specimens (up to 100 nm in thickness) are filled with mineral spikes in native eggshell (E, J), and further suggest that the spikes extend through the mantle and slightly into the core region (D, F, J), as indicated by conventional preparation staining patterns and void morphology within the core region (D, F, Video S9). Additionally, a uniform band of mineral appears to intervene between mantle and core granules (C, H, I arrows).

mammilla covering about 50 μm in length (not all fibers necessarily traverse the mammilla over the entire mammilla diameter), this calculates to collectively 0.5 mm of anchored fiber length. Approximating fiber geometry to a cylinder being 3 μm in diameter, the surface area of the anchored fibers adds up to 5,000 μm^2 (0.005 mm^2). Therefore, the total contact area between the anchored fibers' surface and mammillary calcite is, by a conservative estimate, about 6,500 mm^2, which is very close to the total area of the egg. This appears natural – indeed, the membrane and the shell collectively bound the egg – but it must be kept in mind that at the microscale the orthotropic fibers are aligned with the egg surface, whereas the calcitic mammillae are oriented radially with respect to the egg surface. While the two layers of the shell-membrane complex are parallel/congruent, the structural units of each layer are perpendicular to each other which makes their connection nontrivial. Should the mammillary apices only touch the membrane without 3D embedding/interdigitating, the area of contact would vary between only 10–40% of the total egg surface, depending on the degree of bluntness of the mammillary apices. Moreover, the area of contact between the fibers and the mammillary calcite is further amplified by the fine protrusions of calcite into the fiber mantles in the form of spikes or granules. Since one mineral spike extends into the mantle by about 500 nm, having a typical diameter of 50 nm, then the surface of one spike would be 78,500 nm^2 (0.08 μm^2). With about 100 spikes protruding into every square micrometer of a hypothetically cylindrical fiber mantle surface, the total spikes area is 8 μm^2, which is an increase in the surface area of almost an order of magnitude. In other words, the reciprocal anchorage system of fibers within calcite at the microscale, and of calcite within fibers at the nanoscale, ensures a total organic-inorganic interface area of at least 560 cm^2 per egg.

DISCUSSION

Functional properties of biomineralized tissues and structures are defined by intricate relationships between organic and inorganic constituents, originating from nanometer length scales and in three dimensions[33–35,40–42] – the avian eggshell being no exception. In eggshells, an organic fibrous membrane located between the hard mineralized shell and the soft egg albumen forms an important physical and antimicrobial barrier, while also serving as a substratum for shell formation.[4,21,22] Importantly, unknown features of the membrane determine the spatial distribution of incipient mineral nucleation sites[36] (related to organic cores that attached to the membrane fibers, and become the calcitic mammillae of the shell[21]) that dictate the extent of attachment and the initial trajectory of mineralization. Membrane fibers are oriented orthotropically, like a multilayered mat, in which each fiber roughly follows the curvature of the egg surface. Conversely, the calcitic shell forms from discrete quasiperiodic sites (which will become mammillary apices) scattered over the outer layer of the membrane. Mineral growth then extends radially, forming mammillary bodies and then the palisade columnar layer.[4] The orthotropic membrane fibers and the radial crystal domains are essentially perpendicular to each other, which renders surface congruency intuitively impossible. And yet, following these events in shell formation, not only reliable attachment is enabled, but also protein occlusion into calcite likely ensures adequate dissolution kinetics.[27] Here we described detailed aspects of the eggshell membrane in 3D using submicrometer-resolution μCT and FIB-SEM serial-surface-view electron tomography. Our use of deep learning-assisted segmentation of fibers that differentiates thicknesses across relatively large μCT volumes of up to 1 mm^3 presents a method to assess broadly, and in detail, the intricacy of the membrane fiber and shell mammilla "contact" region. This turns out to be a reciprocal hierarchical assembly on its own account, endowing the natural incubator chamber – the egg – with marvelous functionalities as being *i*) protective against pathogens and yet permeable for gas exchange, *ii*) strong from the outside yet penetrable from the inside (hatching), and *iii*) ensuring calcium flux from the hen to the shell to the chick skeleton.[43,44]

With very high calcium levels in the hen's oviductal fluid, it remains unknown what limits mineralization to the outermost portion of the eggshell membrane yet restricts mineralization elsewhere in the membrane. While the concept of broad default inhibition of mineralization in soft tissues by small biomolecules and proteins in organic fiber systems has been noted, and conversely the promotion of mineralization through the enzymatic degradation of these inhibitors (release from inhibition) – as summarized by the *Stenciling Principle* for mineralization[45,46] – there is no clear explanation yet for how the majority of the membrane fibers remain unmineralized. Evidence best supporting

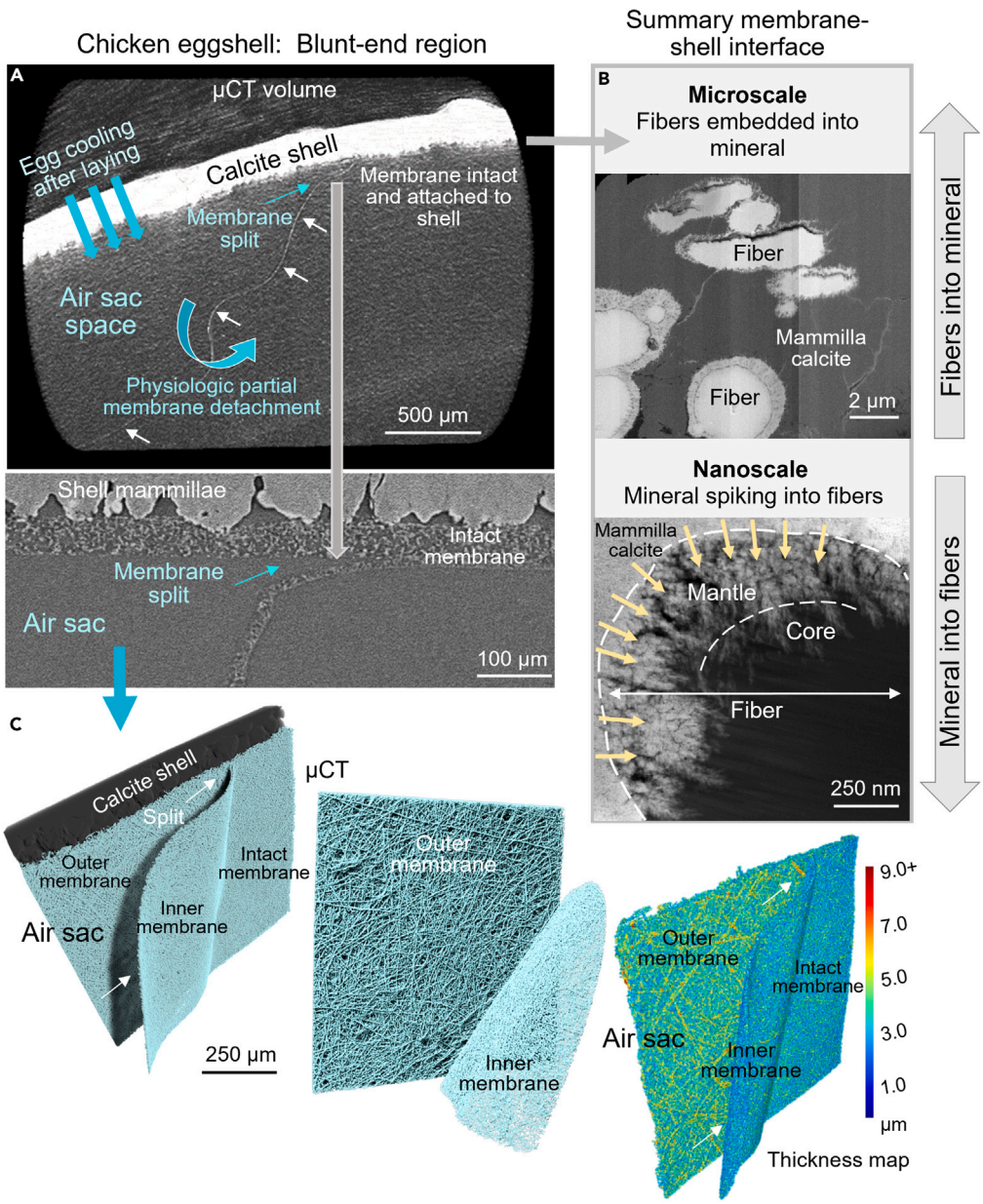

Figure 5. Summary describing multi-scale, self-affine and reciprocal attachment of organic fibers to eggshell mineral: A morphological basis for membrane fiber anchorage underlying air sac formation

(A and B) Summary depiction of chicken eggshell-membrane relationships forming the structural basis for fiber attachment to the avian calcitic shell. During transit in the hen's oviduct (prior to laying), eggshell membrane fibers become anchored into mineral, and mineral penetrates into fiber mantles, collectively securing a strong reciprocal attachment. After an egg is laid, cooling from loss of internal body warmth from the hen results in air ingress through shell pores into the egg to form an air sac at the blunt end of the egg (where pores are more numerous) and which continues to increase in volume over time, and provides oxygen to the developing chick. Using a low-resolution scout μCT scan, the exact coordinates of the membrane split were found (A, Figure S2) and used to image this location at high resolution (C, also see Video S10). The split occurs exactly at the interface between inner (thinner) and outer (thicker) membrane fiber layers, shown here in 2D and 3D, where the outer and inner membrane fibers detach from each other, with an intact (yet to be split) portion of membrane still clearly visible adjacent to the shell (A, C). Splitting of the membrane in thickness at the blunt end of eggs, rather than complete detachment from the mammillae, is ensured by anchorage of outer membrane fibers to the shell (A, left side lower panel and Video S10, see remaining fiber anchorage to the mammillae). The present study provides a morphological basis for understanding how robust attachment is achieved between organic fibers and mineral over multiple length scales, critical not only for air sac formation, but also for association of the underlying chorioallantoic membrane that facilitates eventual shell dissolution, and for overall shell strength. In panel B, brightness variations result from changes in acquisition settings to adjust for sample charging.

the notion of inhibition of fiber mineralization in the avian egg is by *in vitro* biomimetic studies describing great difficulty in prompting intrafibrillar biomimetic mineralization of shell membrane fibers.[47] Recently, this difficulty was overcome through the use of polycarboxylic acid analogues bioinspired by similar protein chemistries operating at the level of mineralization regulation in a variety of marine and terrestrial organisms, and in various *in vitro* model systems.[47] These and other negatively charged proteins and peptides associate with metastable amorphous mineral phases[21] to form transient liquid-like precursors,[48] and their degradation by enzymes likely facilitates mineralization; such enzymes may be largely absent in the milieu of the eggshell membrane.

Here we show using a combination of cryogenic specimen preparation methods and electron imaging, diffraction, and spectral mapping, that the mineralization of eggshell membrane fiber mantle and core regions does occur naturally in the specific instances where fibers interdigitate with, or are embedded within, shell mammilla mineral. In building upon the early work done by Dennis et al.,[9] we describe in three dimensions and at the nanoscale, the spatial extent of this membrane fiber mineralization which forms the morphological basis of the eggshell attachment zone. This interface is spatially and specifically delineated by a unique thin membrane (Figure S1) whose outermost fibers are embedded within shell mineral, and where in turn shell mineral reciprocally penetrates into the fibers as mineral spikes and granules. Such a "pinning/nailing" mechanism at the nanoscale likely provides firm attachment strength by anchoring and preventing untimely detachment of the fibers, thus preventing membrane separation from the shell. Future studies of developing eggs prior to laying, dissected from the shell gland at various stages of shell development, are necessary to determine whether mineralization is initiated first within the fiber core and mantle to proceed outwards, or conversely, whether initiating amongst other organics that broadly comprise the organic mammillary "tips/knobs" (where there could be less inhibition). Mineralization in the mammillary tips would then proceed into the fibers with delicate granule and spike morphologies now influenced by organic constituents of the fibers themselves (we believe this latter scenario to be more likely). Also important to such studies would be the use of cryo-preservation methods to capture any amorphous or otherwise mineral phase transitions during granule/spike maturation. Unraveling the organic determinants of such fine mineral morphologies could contribute to bioinspired or bioengineered designs of interface and/or hybrid composite structures tailored from the nanoscale.

In conclusion, and in broader terms, in biological systems where there is a limited inventory of available materials, attachment between highly dissimilar substances such as unmineralized and mineralized fiber systems requires unique structural adaptations to mitigate the accumulation of critical stresses at and near the interface.[49] With this in mind, biological structure (as it originates from atoms through the nanoscale, and in three dimensions), is often vastly more complex than engineered materials, especially for organisms that incorporate mineralized tissues where water, proteins, and minerals (and of course many other constituents) interact over time to achieve different phases and morphologies.[50,51] This self-affine, reciprocal anchorage system of having organic fibers penetrating bulk mineral at the microscale, and with mineral spikes penetrating organic fibers at the nanoscale (fibers-into-mineral and mineral-into-fibers) provides a morphological basis for understanding the membrane-shell attachment mechanism important to avian eggshell integrity and chick embryonic growth.

Limitations of the study

As applied here, FIB-SEM serial-surface-view (Slice & View) imaging provides critical 3D nano-to microscale context when combined appropriately with lower-resolution techniques that first indicate the broader occurrence of an identified morphological feature. Despite adding essential context using such correlative imaging approaches, the preparation, acquisition, and analysis of 3D FIB-SEM data is a laborious process still providing only a relatively small field-of-view. For any given study analyzed in this way, a limited number of samples can be evaluated by such small-scale electron microscopy techniques. Beyond this, future studies are required that characterize the features we have shown for the domestic chicken in additional avian eggshell types from different species, particularly where nanoscale resolution is required (to date, we have identified fiber interdigitation in at least a similar manner to some degree also in Guinea fowl, quail, and duck eggs, as assessed in preliminary micro-CT volumes – data not shown). Here we present data based on two sample processing techniques (conventional and stained specimens, cryo-prepared unstained specimens) that show mineral spiking into the fiber mantle and core. Additional work should be continued using other advanced cryopreservation techniques, and they should also be applied to eggshells at different stages of development and in different species.

STAR★METHODS

Detailed methods are provided in the online version of this paper and include the following:

- KEY RESOURCES TABLE
- RESOURCE AVAILABILITY
  - Lead contact
  - Materials availability
  - Data and code availability
- EXPERIMENTAL MODEL AND STUDY PARTICIPANT DETAILS
- METHOD DETAILS
  - X-Ray micro-computed tomography (μCT)
  - FIB-SEM operating in serial-surface-view mode
  - Segmentation and image analysis
  - S/TEM and TEM imaging
- QUANTIFICATION AND STATISTICAL ANALYSIS

SUPPLEMENTAL INFORMATION

Supplemental information can be found online at https://doi.org/10.1016/j.isci.2023.108425.

ACKNOWLEDGMENTS

We thank the staff of the Facility for Electron Microscopy Research for assistance with this work, particularly K. Sears, W. Leelapornpisit, D. Liu, and S. Bessette, we thank the staff of the Integrated Quantitative Biology Initiative, and we thank J. Deering for helpful discussions. N.R. and M.D.M. are members of the Québec FRQ-S Centre de Recherche en Biologie Structurale, the Québec FRQ-S Réseau de Recherche en Santé Buccodentaire et Osseuse, and the McGill Institute for Advanced Materials. We also thank Comet Technologies Canada Inc. (Montreal, formerly Objects Research Systems Inc.) for the free-of-charge academic license for the Dragonfly software.

Funding

This study was funded by a Natural Sciences and Engineering Research Council of Canada grant (RGPIN-2022-03238) to M.D.M, a Canada Research Chairs grant (CRC-2018-00199) to M.D.M., and a Québec FRQ-S Réseau de Recherche en Santé Buccodentaire et Osseuse studentship to D.J.B.

AUTHOR CONTRIBUTIONS

M.D.M., N.R., and D.J.B. designed the research. D.J.B. performed the research. M.D.M., N.R., and D.J.B. analyzed the data. D.J.B. wrote the first draft of the article and prepared the first draft of the figures. All the authors edited and commented upon the article and figures.

DECLARATION OF INTERESTS

All the authors declare that they have no competing interests.

Received: September 26, 2023
Revised: October 15, 2023
Accepted: November 7, 2023
Published: November 9, 2023

REFERENCES

1. Riley, A., Sturrock, C.J., Mooney, S.J., and Luck, M.R. (2014). Quantification of eggshell microstructure using X-ray micro computed tomography. Br. Poultry Sci. *55*, 311–320.
2. Rahn, H., Ar, A., and Paganelli, C.V. (1979). How Bird Eggs Breathe. Sci. Am. *240*, 46–55.
3. Rahn, H., Paganelli, C.V., and Ar, A. (1987). Pores and gas exchange of avian eggs: a review. J. Exp. Zool. Suppl. *1*, 165–172.
4. Hincke, M.T., Nys, Y., Gautron, J., Mann, K., Rodriguez-Navarro, A.B., and McKee, M.D. (2012). The eggshell: structure, composition and mineralization. Front. Biosci. *17*, 1266–1280.
5. Romanoff, A.L., and Romanoff, A.J. (1949). The Avian Egg (J. Wiley).
6. Tan, C.K., Chen, T.W., Chan, H.L., and Ng, L.S. (1992). A scanning and transmission electron microscopic study of the membranes of chicken egg. Histol. Histopathol. *7*, 339–345.
7. Bellairs, R., and Boyde, A. (1969). Scanning electron microscopy of the shell membranes of the hen's egg. Z. Zellforsch. Mikrosk. Anat. *96*, 237–249.
8. Damaziak, K., and Marzec, A. (2022). Analysis of ultrastructure and microstructure of blackbird (Turdus merula) and song thrush (Turdus philomelos) eggshell by scanning electron microscopy and X-ray computed microtomography. Sci. Rep. *12*, 11857.
9. Dennis, J.E., Xiao, S.Q., Agarwal, M., Fink, D.J., Heuer, A.H., and Caplan, A.I. (1996). Microstructure of matrix and mineral components of eggshells from White Leghorn chickens (Gallus gallus). J. Morphol. *228*, 287–306.
10. BALCH, D.-A., and COOKE, R.,A. (1970). A STUDY OF THE COMPOSITION OF HEN'S EGG-SHELL MEMBRANES. Ann. Biol. Anim. Biochim. Biophys. *10*, 13–25.
11. Leach, R.M. (1982). Biochemistry of the Organic Matrix of the Eggshell1. Poultry Sci. *61*, 2040–2047.
12. Harris, E.D., Blount, J.E., and Leach, R.M., Jr. (1980). Localization of lysyl oxidase in hen oviduct: implications in egg shell membrane formation and composition. Science *208*, 55–56.
13. Wong, M., Hendrix, M.J., von der Mark, K., Little, C., and Stern, R. (1984). Collagen in the egg shell membranes of the hen. Dev. Biol. *104*, 28–36.
14. Arias, J.L., Fernandez, M.S., Dennis, J.E., and Caplan, A.I. (1991). Collagens of the chicken eggshell membranes. Connect. Tissue Res. *26*, 37–45.
15. Ahmed, T.A.E., Suso, H.P., and Hincke, M.T. (2017). In-depth comparative analysis of the chicken eggshell membrane proteome. J. Proteonomics *155*, 49–62.
16. Hincke, M.T., Chien, Y.C., Gerstenfeld, L.C., and McKee, M.D. (2008). Colloidal-gold immunocytochemical localization of osteopontin in avian eggshell gland and eggshell. J. Histochem. Cytochem. *56*, 467–476.
17. Le Roy, N., Stapane, L., Gautron, J., and Hincke, M.T. (2021). Evolution of the Avian Eggshell Biomineralization Protein Toolkit - New Insights From Multi-Omics. Front. Genet. *12*, 672433.
18. Hincke, M.T., Gautron, J., Panheleux, M., Garcia-Ruiz, J., McKee, M.D., and Nys, Y. (2000). Identification and localization of lysozyme as a component of eggshell membranes and eggshell matrix. Matrix Biol. *19*, 443–453.
19. Nys, Y., Gautron, J., Garcia-Ruiz, J.M., and Hincke, M.T. (2004). Avian eggshell mineralization: biochemical and functional characterization of matrix proteins. Comptes Rendus Palevol *3*, 549–562.
20. Dauphin, Y., Cuif, J.-P., Salomé, M., Susini, J., and Williams, C.T. (2006). Microstructure and chemical composition of giant avian eggshells. Anal. Bioanal. Chem. *386*, 1761–1771.
21. Rodríguez-Navarro, A.B., Marie, P., Nys, Y., Hincke, M.T., and Gautron, J. (2015). Amorphous calcium carbonate controls avian eggshell mineralization: A new paradigm for understanding rapid eggshell calcification. J. Struct. Biol. *190*, 291–303.
22. Gautron, J., Stapane, L., Le Roy, N., Nys, Y., Rodriguez-Navarro, A.B., and Hincke, M.T. (2021). Avian eggshell biomineralization: an update on its structure, mineralogy and protein tool kit. BMC Mol. Cell Biol. *22*, 11.
23. Bunk, M.J., and Balloun, S.L. (1977). Structure and relationship of the mammillary core to membrane fibres and initial calcification of the avian Egg Shell. Br. Poultry Sci. *18*, 617–621.
24. Li, Y., Li, Y., Liu, S., Tang, Y., Mo, B., and Liao, H. (2018). New zonal structure and transition of the membrane to mammillae in the eggshell of chicken Gallus domesticus. J. Struct. Biol. *203*, 162–169.
25. Halgrain, M., Georgeault, S., Bernardet, N., Hincke, M.T., and Réhault-Godbert, S. (2022). Concomitant Morphological Modifications of the Avian Eggshell, Eggshell Membranes and

the Chorioallantoic Membrane During Embryonic Development. Front. Physiol. *13*, 838013.
26. Chien, Y.C., Hincke, M.T., and McKee, M.D. (2009). Ultrastructure of avian eggshell during resorption following egg fertilization. J. Struct. Biol. *168*, 527–538.
27. Athanasiadou, D., Jiang, W., Goldbaum, D., Saleem, A., Basu, K., Pacella, M.S., Böhm, C.F., Chromik, R.R., Hincke, M.T., Rodríguez-Navarro, A.B., et al. (2018). Nanostructure, osteopontin, and mechanical properties of calcitic avian eggshell. Sci. Adv. *4*, eaar3219.
28. Tyler, C., and Simkiss, K. (1959). Studies on egg shells. XII.—Some changes in the shell during incubation. J. Sci. Food Agric. *10*, 611–615.
29. Örberg, J. (1990). Relationship between the shell membrane-shell bond and shell deformation in hens' eggs. Br. Poultry Sci. *31*, 249–254.
30. Liu, F., Jiang, X., and Wang, L. (2022). Mechanical Design Principles of Avian Eggshells for Survivability. Preprint at arXiv.
31. Berrang, M.E., Cox, N.A., Frank, J.F., and Buhr, R.J. (1999). Bacterial Penetration of the Eggshell and Shell Membranes of the Chicken Hatching Egg: A Review. J. Appl. Poultry Res. *8*, 499–504.
32. Ray, A., Roberts, J.R., Flavel, R., and Chousalkar, K.K. (2015). Eggshell penetration by Salmonella Typhimurium in table eggs: Examination of underlying eggshell structures by micro-computed tomography and scanning electron microscopy. Food Res. Int. *78*, 34–40.
33. Zou, Z., Tang, T., Macías-Sánchez, E., Sviben, S., Landis, W.J., Bertinetti, L., and Fratzl, P. (2020). Three-dimensional structural interrelations between cells, extracellular matrix, and mineral in normally mineralizing avian leg tendon. Proc. Natl. Acad. Sci. USA *117*, 14102–14109.
34. Buss, D.J., Reznikov, N., and McKee, M.D. (2020). Crossfibrillar mineral tessellation in normal and Hyp mouse bone as revealed by 3D FIB-SEM microscopy. J. Struct. Biol. *212*, 107603.
35. Buss, D.J., Rechav, K., Reznikov, N., and McKee, M.D. (2023). Mineral tessellation in mouse enthesis fibrocartilage, Achilles tendon, and Hyp calcifying enthesopathy: A shared 3D mineralization pattern. Bone *174*, 116818.
36. Park, J.A., and Sohn, S.H. (2018). The Influence of Hen Aging on Eggshell Ultrastructure and Shell Mineral Components. Korean J. Food Sci. Anim. Resour. *38*, 1080–1091.
37. Lei, C., Wang, Y.H., Zhuang, P.X., Li, Y.T., Wan, Q.Q., Ma, Y.X., Tay, F.R., and Niu, L.N. (2022). Applications of Cryogenic Electron Microscopy in Biomineralization Research. J. Dent. Res. *101*, 505–514.
38. Narushin, V.G. (2005). Egg geometry calculation using the measurements of length and breadth. Poultry Sci. *84*, 482–484.
39. Paganelli, C.V., Olszowka, A., and Ar, A. (1974). The Avian Egg: Surface Area, Volume, and Density. Condor *76*, 319–325.
40. Buss, D.J., Kröger, R., McKee, M.D., and Reznikov, N. (2022). Hierarchical organization of bone in three dimensions: A twist of twists. J. Struct. Biol. X *6*, 100057.
41. Fratzl, P., and Weinkamer, R. (2007). Nature's hierarchical materials. Prog. Mater. Sci. *52*, 1263–1334.
42. Zhou, J., Wang, S., Nie, F., Feng, L., Zhu, G., and Jiang, L. (2011). Elaborate architecture of the hierarchical hen's eggshell. Nano Res. *4*, 171–179.
43. Solomon, S.E. (2010). The eggshell: strength, structure and function. Br. Poultry Sci. *51* (*Suppl 1*), 52–59.
44. Bain, M.M. (1992). Eggshell strength: A relationship between the mechanism of failure and the ultrastructural organisation of the mammillary layer. Br. Poultry Sci. *33*, 303–319.
45. Reznikov, N., Hoac, B., Buss, D.J., Addison, W.N., Barros, N.M.T., and McKee, M.D. (2020). Biological stenciling of mineralization in the skeleton: Local enzymatic removal of inhibitors in the extracellular matrix. Bone *138*, 115447.
46. McKee, M.D., Buss, D.J., and Reznikov, N. (2022). Mineral tessellation in bone and the stenciling principle for extracellular matrix mineralization. J. Struct. Biol. *214*, 107823.
47. Li, N., Niu, L.N., Qi, Y.P., Yiu, C.K.Y., Ryou, H., Arola, D.D., Chen, J.H., Pashley, D.H., and Tay, F.R. (2011). Subtleties of biomineralisation revealed by manipulation of the eggshell membrane. Biomaterials *32*, 8743–8752.
48. Gower, L.B., and Odom, D.J. (2000). Deposition of calcium carbonate films by a polymer-induced liquid-precursor (PILP) process. J. Cryst. Growth *210*, 719–734.
49. Thomopoulos, S., Birman, V., and Genin, G. (2013). The Challenge of Attaching Dissimilar Materials in Structural Interfaces and Attachments in Biology (Springer), pp. 3–17.
50. Mann, S., and Weiner, S. (1999). Biomineralization: structural questions at all length scales. J. Struct. Biol. *126*, 179–181.
51. Weiner, S., Sagi, I., and Addadi, L. (2005). Structural biology. Choosing the crystallization path less traveled. Science *309*, 1027–1028.
52. Reznikov, N., Buss, D.J., Provencher, B., McKee, M.D., and Piché, N. (2020). Deep learning for 3D imaging and image analysis in biomineralization research. J. Struct. Biol. *212*, 107598.

STAR★METHODS

KEY RESOURCES TABLE

REAGENT or RESOURCE	SOURCE	IDENTIFIER
Antibodies		
Rabbit polyclonal anti-chicken osteopontin	Dr. Louis C. Gerstenfeld	Boston University
Biological samples		
Avian chicken eggshells	Commercially available, North American chicken breeders	
Chemicals, peptides, and recombinant proteins		
Paraformaldehyde	Thermo Fisher Scientific	AC416785000
Glutaraldehyde	Electron Microscopy Sciences	16210
Sodium cacodylate buffer	Electron Microscopy Sciences	12310
Potassium ferrocyanide	Sigma-Aldrich	P9387
Osmium tetroxide	Electron Microscopy Sciences	19150
Experimental models: Organisms/strains		
Commercially available chicken eggshells, from North American chicken breeders		
Software and algorithms		
Dragonfly	Comet Technologies Canada Inc., Montreal (formerly Object Research Systems Inc.)	

RESOURCE AVAILABILITY

Lead contact

Further information and inquiries should be directed to and will be fulfilled by the lead contact, Marc McKee (marc.mckee@mcgill.ca).

Materials availability

Commercially available eggshells were acquired from North American breeders.

Data and code availability

Data: All data reported in this paper will be shared by the lead contact upon request.

Code: Not applicable.

Any additional information required to reanalyze the data reported in this paper is available from the lead contact upon request.

EXPERIMENTAL MODEL AND STUDY PARTICIPANT DETAILS

Unfertilized and unincubated chicken (*Gallus gallus domesticus*) eggs were acquired from North American breeders. Although laying hen information was not obtained for each egg analyzed, overall structural characteristics of each egg were assessed by optical microscopy such that all samples analyzed were consistent with each other and with observations from prior studies.[1,36]

METHOD DETAILS

X-Ray micro-computed tomography (μCT)

Fresh unfertilized and unincubated (and therefore unhatched) chicken eggs were carefully opened from above the equatorial region (near the pointed end of the egg) and the inner contents were drained. The remaining shell and attached membrane were gently and quickly rinsed from the inside with several rounds of tap water (with gentle swirling motion) for about 2 minutes to remove any remaining inner egg contents. Small pieces of shell (approximately 5 mm × 5 mm) were cut from the equatorial region using a sharp dissecting scissor, and the best-cut pieces were chosen for μCT imaging. After drying overnight, intact shell and attached membrane pieces were imaged using an X-ray micro-computed tomography scanner Xradia Versa 520 (Carl Zeiss, Oberkochen, Germany) having submicrometer resolution. "Scout" lower-resolution warmup scans were performed with a 0.4x objective lens to ensure that final high-resolution scans would be located centrally within each specimen ("Scout and Zoom" method, Carl Zeiss, Oberkochen, Germany). High-resolution scans were performed with a 4x objective lens, 60kV source voltage, and an exposure of 5s per projection. Detector and source distances were optimized to create a voxel size of 500 nm with no binning. 3000+ projections were obtained for each high resolution scan. Additional separate specimens from the equatorial

region were subject to mechanical removal of the membrane by hand, this after the rinsing step and while still hydrated. The membrane was confirmed to be removed by a dissecting light microscope, this as compared to specimens with the membrane left intact.

For 3D imaging of the membrane split to form the air sac at the blunt end of the egg, a similar workflow for specimen dissection was employed. The air sac and membrane split are visible under a dissecting microscope and by eye. After careful washing, and then removal of shell above the split, the site of the physiologic membrane split could be preserved. A significant portion of the shell above and below the split was left intact so as not to disturb the split site of interest (Figure S2). To secure the inner membrane during scanning, a very small drop of strong adhesive was painted onto the topmost portion of the shell fragment (significantly outside the volume to be scanned), and the free end of the inner membrane "flap" was then gently secured at this position (Figure S2). These specimens were also left to dry overnight and imaged with the same conditions as above. Since the inner membrane is only 10–15 μm thick, the "Scout and Zoom" method was critical to finding the exact coordinates of the split, then allowing for high-resolution imaging at this precise location (Figure S2).

FIB-SEM operating in serial-surface-view mode

Four focused ion beam scanning electron microscope (FIB-SEM) serial-surface-view volumes were obtained at different resolutions to characterize the eggshell membrane and its attachment to the calcite shell mammillae. Eggs were drained and rinsed with tap water in the same manner as above, and then chemically fixed with 4% paraformaldehyde (Thermo Fisher Scientific) and 1% glutaraldehyde (Electron Microscopy Sciences, Hatfield, PA, USA) in 0.1 M sodium cacodylate buffer (pH 7.3, Electron Microscopy Sciences, Hatfield, PA, USA) for 1 hour. After washing in additional 0.1 M sodium cacodylate buffer, specimens were stained with 4% potassium ferrocyanide-reduced osmium tetroxide. Graded dehydration to 100% pure acetone was then followed by gradual infiltration with Epon resin over several days. Final polymerization in pure Epon was achieved over 2 days at 60°C. Cured Epon blocks were manually trimmed to a suitable plane within the embedded eggshell, and then the blockfaces were polished using a Struers LaboSystem polisher. Semi-manual polishing was done without using the LaboSystem head. A series of polishing steps was applied for approximately 5–10 minutes of polishing per stage. Each mat was rinsed with water and dampened before addition of slurry and lubricant. The specimen was briefly rinsed in a sonicator between each polishing step. After polishing, the block was attached to a metallic stub, coated with a 5-nm layer of Pt on the polished face, and imaged initially using SEM-BSE to define a suitable region of interest. FIB-SEM serial-surface-view imaging was conducted using an FEI Helios Nanolab 660 (first 2 volumes), and a Hitachi Ethos NX5000 (2 other volumes, and lamella preparation as explained below). Volumes 1 (Figure S1) and 2 (Figures 1D, 1E, 2C, 2D, and 3D, Videos S3, S4, S5, and S7) were collected with conditions of 2 kV imaging voltage and 0.79 nA milling current with slice thicknesses of 41 nm and 70 nm, respectively, achieving isotropic voxel resolutions over total volumes of 36,132 μm^3 (approximately 64 × 43 × 13 μm) and 328,530 μm^3 (approximately 111 × 73 × 41 μm). To achieve such a large volume in Volume 2, the length of the eggshell membrane was oriented parallel to the direction of the ion beam (Figure S2). Electron imaging on the opposite face was conducted within a few μms of the ledge so as to avoid heavy curtaining artifacts. Volumes 3 (Figures 3E, 3F, and 4A, Video S8) and 4 (Figure 3E rightmost image; Figures 4D and 4J [except for cryo-prep image]) were collected on the Hitachi Ethos NX5000 using a 2 kV source voltage 1.5 nA milling current, with image formation occurring separately from both upper and lower backscattered electron populations simultaneously (BSE-U and BSE-L detectors, see Figures 4A and 4D). Slice thicknesses of these volumes were both 14 nm, with volume 3 x/y resolution at 12.5 nm, and Volume 4 continuing for some additional time with x/y resolution 6 nm, to achieve final volumes of 2,739 μm^3 (approximately 16 × 14 × 13 μm) and 48 μm^3 (approximately 6 × 6 × 1.3 μm), respectively. Each stack of images was registered and aligned in Dragonfly using the slice registration toolkit "mutual info" algorithm. Nonisotropic Volumes 3 and 4 were registered with correct pixel sizes to create accurate 3D segmentations.

Segmentation and image analysis

Dragonfly image analysis software with deep learning capabilities (Comet Technologies Canada Inc., Montreal, formerly Object Research Systems Inc.) was used to analyze all image data. To assess overall morphological differences between inner and outer membrane fibers of Micro-CT data, and to segment the calcite shell in these acquired volumes of nearly 1 mm^3 at a resolution of 500 nm/voxel, deep learning-based segmentation was employed. From several projections of the *en face* view of the membrane (derived as a new dataset into the image plane), segmentation of "ground truth" slices was carried out using the range and ROI painter tools. Additional separate "ground truth" examples were taken of embedded fiber tracts (also of lower overall grayscale values than the surrounding calcite). A mask ROI was created to label each slice that was manually segmented. For each region (normal membrane fibers and embedded fiber tracts), a separate convolutional neural network (CNN) was generated with an architecture having a depth of 5 layers and 64 convolutional filters per layer (and with inputs being partitioned into learning [80%] and validation [20%] subsets). Training parameters were patch size of 64, the S:I ratio was 0.5, and the batch size was 64. Training continued until no improvement was made for 10 epochs. After initial segmentation, corrections were made on different slices, and the models were further refined in an additional round of training. This approach was demonstrated recently in a review with case studies with special emphasis on mineralized tissues (including eggshell).[52] Both normal fibers and fiber tract segmentation labels were combined into one, thus labeling all of the membrane fibers including those interfacing with and within shell mammillae calcite. For select volumes, only the fiber tracts (embedded and interfacing fibers) are shown. For other select volumes thickness mapping was applied using Dragonfly software after 3 rounds of smoothing (k = 3) to reduce computational expense.

To segment stained fibers, fiber mantle and core regions, and calcite mammillae of FIB-SEM volumes, a similar deep learning-based approach to the Micro-CT data was utilized. Briefly, 1–2% of total image slices from each FIB-SEM stack were manually segmented using Dragonfly ROI painter tools. Corrected slices were provided as training input for a convolutional neural network (CNN), again using default architecture (depth of 5 layers and 64 convolutional filter per layer). Training parameters were the same as above, except for batch and patch

sizes of 32. Training stopped after 10 consecutive epochs with no improvement in learning (based on the training/validation loss convergence. Different semantic segmentation models were trained for each target class – for example, fiber mantle vs. core vs. mammillae. The model for the largest volume of the membrane in full cross-section was trained to recognized and ignore minor bright curtaining artifacts toward the far edge of the volume. Three rounds of object smoothing were applied to each segmentation output (kernel = 3). This is a minimum smoothing step and is designed to reduce computational expense for subsequent analyses. Volume thickness maps were also created of select FIB-SEM segmentations and cropped regions from these segmentations using the "volume thickness map" operation. This operation computes maximum possible diameters within 3D foreground features. Sphere diameters are then color coded and also displayed as histogram distributions for appropriate panels. Shadowing effects are used to highlight texture and orientations of FIB-SEM 3D segmentations. Directionality mapping was completed with the Dragonfly software Bone Analysis plugin using a surface normal algorithm and segmentation input of the full membrane in cross-section.

To approximate what the surface area of a theoretical "nonspiked" mantle would be (as it would interface directly to mammilla calcite), a cylinder was created in Dragonfly and modified to have its curved dimension approximating the overall true spiked fiber mantle curvature (shown in Figure 4J). While the cylinder was selected, the view mode was changed to a nonplanar view. From this view, multislice painting with the smallest brush was used to label this curvature as a thin plane approximating an equivalent smooth mantle curvature. The surface area of mantle spikes/voids from Figure 4J was then compared to the surface area of the theoretical nonspiked thin plane to determine the magnitude difference in the inorganic-organic attachment area provided by the mineral spikes in native eggshell.

S/TEM and TEM imaging

Sample preparation

- Lamella 1 – Conventional preparation:

From the same block as FIB-SEM Volume 3, front and back trenches were progressively milled into the blockface at the tip of a different selected mammilla to create a thin lamella where several mammilla-embedded and interfacial fibers were visible. A standard lift-out technique using the Hitachi Ethos NX5000 FIB-SEM was used to trim the lamella to a final thickness of around 250 nm (Gallium milling at 30 keV, 1.5 nA; 30 keV, 280 pA; 15 keV, 100 pA; and 10keV, 50pA; with each step being applied to both faces of the lamella). Sequential reduction in current and voltage was applied to decrease contamination and an amorphous gallium layer in the lamella. A final step of 210 s of Argon (each face receiving half this duration) at 2 keV was applied to eliminate any residual gallium.

- Lamella 2 – Cryo-preparation:

Different chicken eggshells were rinsed and briefly washed in the same manner as mentioned in the sections for X-ray and FIB-SEM specimens. Exactly following this, eggshell pieces (with membrane) were placed in a dish with cryoprotectant (hexadecane), and placed in a vacuum for 30 min. Within 2 h, all eggshell pieces were cryo-fixed using a Leica EM ICE (Leica, Wetzlar, Germany), and samples were subsequently dehydrated into pure acetone by freeze substitution in a Leica ASF2. Standard infiltration and embedding in Epon resin, and block preparation were conducted as outlined in the FIB-SEM section above. Lamella preparation of this cryo-prepared specimen was carried out similar to Lamella 1 above using the Hitachi Ethos NX5000 FIB-SEM.

- Decalcified sections and immunogold labeling for osteopontin:

Equatorial-region eggshell samples with attached eggshell membrane were chemically fixed with 4% paraformaldehyde (Thermo Fisher Scientific) and 1% glutaraldehyde (Electron Microscopy Sciences, Hatfield, PA, USA) in 0.1 M sodium cacodylate buffer (pH 7.3, Electron Microscopy Sciences, Hatfield, PA, USA) for 1 h. After washing briefly in additional 0.1 M sodium cacodylate buffer, specimens were decalcified in 8% EDTA, and then gradient-dehydrated to 100% pure ethanol, and then gradually infiltrated and embedded in LR White acrylic resin (Electron Microscopy Sciences, Hatfield, PA, USA). Final polymerization in pure LR White was achieved over 2 days at 60°C. Cured resin blocks were manually trimmed to a suitable plane within the embedded eggshell, and microtomed with a diamond knife for light microscopy at 0.5-µm-thickness, or at 80-nm-thickness for TEM using a Leica Ultracut E ultramicrotome. For immunogold labeling and TEM, grid-mounted sections were incubated with anti-chicken polyclonal osteopontin antibody (courtesy of Dr. Louis Gerstenfeld) followed by protein A-gold conjugate (14 nm gold particle size, from G. Posthumus, University of Utrecht, The Netherlands). Labeled grids were then conventionally stained with uranyl acetate and lead citrate.

Imaging

Transmission (TEM) and scanning transmission electron (S/TEM) microscopy were performed on conventional and cryo-prepared specimens. TEM imaging was conducted using a Talos F200X S/TEM microscope (Thermo Fisher Scientific) equipped with a 4k x 4k Ceta 16M CMOS camera and operating at 200 kV, and using a 40 µm objective aperture. Diffraction patterns were collected after removing the objective aperture, changing the camera mode to HDR with a camera length of 330 mm, and inserting a selected area aperture (270 nm). For EDS mapping, a unique STEM field emission gun register was utilized (changing the gun length to 3, and spot size 6), and camera length was set to 98 mm with no aperture inserted. A spectrum image area containing features typical of mammilla, mantle, and core (of the cryo-prepared lamella) was created alongside a separate smaller drift area. Spectra intensities were recorded for 15 min as maps for Ca, O, and C. High-resolution

STEM imaging (gun length = 5, spot size 9) of mineralized fiber morphology was also conducted on the Talos F200X using a high-angle annular dark-field (HAADF) detector (collecting only electrons scattered to 58–200 mrad).

QUANTIFICATION AND STATISTICAL ANALYSIS

Dragonfly image analysis software with deep learning capabilities (Comet Technologies Canada Inc., formerly Object Research Systems Inc., Montreal, QC, Canada) was used to segment and analyze all image data (used for segmentation in Figures 1, 2, 3, 4, and 5; Figure S1). Details of this process can be read in the "segmentation and image analysis" section, and also in a recent review with case studies on the use of deep learning for 3D imaging in biomineralization studies.[52] The thickness mapping operation in the software computes maximal fitting diameters within 3D foreground features. Sphere diameters were then automatically color coded as part of the available plugin *Thickness Map*, and also displayed as histogram distributions for appropriate panels (analysis used in Figures 1, 3, 4, and 5). Directionality 3D vector mapping was completed with the Dragonfly software Bone Analysis plugin using a surface-normal algorithm and segmentation input of the full membrane in cross-section (analysis used in Figure 1).

Quantitation via sphere thickness mapping and corresponding histogram distributions of mapped sphere values were computed and plotted directly in the Dragonfly software (values taken directly from raw and/or segmented data). Histograms were exported from Dragonfly into.tiff files shown in Figure 1 panel B and D, Figure 3 panel F, Figure 4 panel J, and Figure 5 panel C. In Figure 1 panel D, M represents the arithmetic average of the dataset, and Mdn represents the value at which half the recorded sphere thicknesses fall below and half above. In Figure 2D, pie charts were created from the volume of each segmented region (mantle, core, and interfibrillar space). These values were exported to a Microsoft Excel file and plotted. All other data figures and panels, and this paper's main findings, are validated through detailed imaging study and correlative descriptive analysis across multiple scales.